Published on 18 April 2016. Downloaded by TU Berlin - Universitaetsbibl on 18/05/2017 14:53:02.

Energy & Environmental Science

ROYAL SOCIETY OF CHEMISTRY

PAPER

View Article Online
View Journal | View Issue

Cite this: *Energy Environ. Sci.*, 2016, **9**, 1818

Annihilation of structural defects in chalcogenide absorber films for high-efficiency solar cells†

Roland Mainz,*[a] Ekin Simsek Sanli,[b] Helena Stange,[c] Doron Azulay,[d] Stephan Brunken,[a] Dieter Greiner,[a] Shir Hajaj,[d] Marc D. Heinemann,[a] Christian A. Kaufmann,[a] Manuela Klaus,[a] Quentin M. Ramasse,[e] Humberto Rodriguez-Alvarez,[a] Alfons Weber,[a] Isaac Balberg,[d] Oded Millo,[d] Peter A. van Aken[b] and Daniel Abou-Ras[a]

Received 6th February 2016, Accepted 30th March 2016

DOI: 10.1039/c6ee00402d

www.rsc.org/ees

In polycrystalline semiconductor absorbers for thin-film solar cells, structural defects may enhance electron–hole recombination and hence lower the resulting energy conversion efficiency. To be able to efficiently design and optimize fabrication processes that result in high-quality materials, knowledge of the nature of structural defects as well as their formation and annihilation during film growth is essential. Here we show that in co-evaporated $Cu(In,Ga)Se_2$ absorber films the density of defects is strongly influenced by the reaction path and substrate temperature during film growth. A combination of high-resolution electron microscopy, atomic force microscopy, scanning tunneling microscopy, and X-ray diffraction shows that $Cu(In,Ga)Se_2$ absorber films deposited at low temperature without a Cu-rich stage suffer from a high density of – partially electronically active – planar defects in the {112} planes. Real-time X-ray diffraction reveals that these faults are nearly completely annihilated during an intermediate Cu-rich process stage with $[Cu]/([In] + [Ga]) > 1$. Moreover, correlations between real-time diffraction and fluorescence analysis during Cu–Se deposition reveal that rapid defect annihilation starts shortly before the start of segregation of excess Cu–Se at the surface of the $Cu(In,Ga)Se_2$ film. The presented results hence provide direct insights into the dynamics of the film-quality-improving mechanism.

Broader context

The development of thin-film solar cells has been a success story in recent years in terms of record efficiencies in the lab. Single junction solar cells based on compound semiconductor films have reached higher energy-conversion efficiencies than polycrystalline silicon. Despite this success and the prospects of novel applications such as flexible, lightweight solar panels, the market share of thin-film solar modules is stagnating. A major problem of compound thin-film solar cells, such as $Cu(In,Ga)Se_2$, is the large gap between lab efficiencies and commercial module efficiencies. A large process parameter space makes trial-and-error optimization a time-consuming and expensive task. Therefore, understanding the underlying atomic-scale physics and chemistry is essential to identify the potential origins of efficiency losses in the transfer from lab- to large-scale fabrication. Even though $Cu(In,Ga)Se_2$ has been investigated for several decades, there is still a lack of fundamental knowledge of the quality-determining mechanisms during film growth. In this contribution we present results from an international collaboration that provides direct insight into defect formation and annihilation during the fabrication of $Cu(In,Ga)Se_2$ films. Consequences for process optimization and design are proposed. The presented approach can also be applied to understand other thin-film fabrication processes.

1 Introduction

Low-temperature fabrication of semiconductor films for solar cells and other applications reduces the energy consumption during fabrication and enables the use of substrates with limited temperature tolerance, such as light-weight and flexible polyimide foils, and thus has the potential to enhance the competitiveness and scale-up of solar power.[1] A general challenge for low-temperature synthesis, however, is the possible formation of structural disorders induced by growth accidents[2]

[a] *Helmholtz-Zentrum Berlin für Materialien und Energie GmbH, Hahn-Meitner-Platz 1, 14109 Berlin, Germany. E-mail: roland.mainz@helmholtz-berlin.de*
[b] *Max Planck Institute for Solid State Research, Stuttgart Center for Electron Microscopy, Heisenbergstr. 1, 70569 Stuttgart, Germany*
[c] *Technische Universität Berlin, Institut für Werkstoffwissenschaften, Ernst-Reuter-Platz 1, 10587 Berlin, Germany*
[d] *Racah Institute of Physics and the Center for Nanoscience and Nanotechnology, The Hebrew University of Jerusalem, Jerusalem 91904, Israel*
[e] *SuperSTEM Laboratory, SciTech Daresbury Campus, Keckwick Lane, Daresbury, WA4 4AD, UK*

† Electronic supplementary information (ESI) available. See DOI: 10.1039/c6ee00402d

This journal is © The Royal Society of Chemistry 2016

View Article Online

Published on 18 April 2016. Downloaded by TU Berlin - Universitaetsbibl on 18/05/2017 14:53:02.

or incomplete phase transitions,[3] which may deteriorate the device performance and cancel out the aforementioned advantages.[4,5] In many cases these problems can be surpassed by a smart process design. Remarkable success in increasing the power-conversion efficiencies of solar cells based on low-temperature (<500 °C) deposited $Cu(In,Ga)Se_2$ (CIGSe) to the world-record level has been recently achieved.[6,7] Even though a Cu-poor composition ($[Cu]/([In] + [Ga]) < 1$) is needed for high efficiencies, at low temperatures as well as moderate temperatures (~ 530 °C) the synthesis of high-quality CIGSe relies on a complex three-stage co-evaporation process in which the film takes a detour *via* an intermediate Cu-rich composition ($[Cu]/([In] + [Ga]) > 1$).[8] In this process, the optoelectronic properties and solar cell efficiencies are improved by the intermediate Cu-rich process stage, realized by the deposition of Cu–Se in excess.[9,10] Despite the fact that this phenomenon has been known for more than two decades,[8,11,12] the nature of the mechanism responsible for this efficiency improvement is not yet fully accounted for. In this contribution we provide novel insights into the nature and dynamics of the mechanism responsible for the improvement of the film quality during CIGSe growth.

It is well known that in chalcopyrite and kesterite films an increase in Cu concentration up to the formation of secondary Cu–Se compounds promotes grain growth.[8,10–17] Even in sequential CIGSe synthesis by chalcogenization of metallic precursors[18] – where the integral Cu content remains constant during the process – Cu–Se can intermediately form at the surface.[19] It has been shown, however, that CIGSe absorbers with various average grain sizes ranging from about 0.5 μm to more than 1 μm can lead to high power conversion efficiencies of around 20%.[6,7,20] Hence, the mere reduction of the grain boundary area cannot explain the improved efficiencies and it seems likely that the Cu-poor to Cu-rich transition is additionally accompanied by a reduction of detrimental defects within the grains.[13,21] Structural defects such as dislocations and stacking faults were found in CIGSe and Cu_2ZnSnS_4 films using transmission electron microscopy (TEM).[21–26] Yet, no detailed information on the effect of the Cu-poor to Cu-rich transition on the density of planar defects (PDs) is found in the literature. While fascinating insights into annihilation mechanisms of single planar defects in other metallic or compound fcc materials were obtained by time-resolved TEM studies,[27–29] real-time *in situ* TEM in a reactive Cu–Se atmosphere to study defect annihilation in CIGSe does not seem to be feasible. In contrast, X-ray diffraction (XRD) is well suited for real-time analysis in reactive atmospheres[30,31] and it has been predicted that stacking faults in CIGSe cause a characteristic signature in XRD.[15]

In the present study, we combine high-resolution microscopy with real-time X-ray diffraction and fluorescence analysis to study the nature and evolution of PDs in CIGSe during Cu–Se deposition. The presented results provide direct insights into the role of the intermediate Cu-rich process stage in achieving an absorber material with a relatively small concentration of defects for high-efficiency solar cells.

2 Results and discussion

2.1 Characterization of planar defects

Two types of CIGSe films were synthesized in a three-stage co-evaporation process – one with and the other without an intermediate Cu-rich process stage. Both types of samples were processed in the same process run, consisting of Ga–Se and In–Se deposition in the first stage, Cu–Se deposition in the second stage and Ga–In–Se deposition in the third stage, with a maximum substrate temperature of 430 °C. For the samples processed without a Cu-rich stage, the process was interrupted during Cu–Se deposition before the composition turned Cu-rich. For the sample processed with a Cu-rich stage, Cu–Se deposition was continued until a Cu-rich composition was reached, and subsequently the composition turned Cu-poor by final In–Ga–Se deposition. (For more details on the film synthesis see Methods.)

Scanning TEM low-angle annular dark-field (STEM-LAADF) imaging[32] shows that the sample processed without the Cu-rich stage features grain sizes of around 0.5 to 1 μm (Fig. 1a), while the grain size of the sample grown with a Cu-rich stage increased to up to about 2 μm (Fig. 1b). Several of the grains in the sample without a Cu-rich stage feature a high density of extended PDs, visible as parallel stripes[33] (Fig. 1a, marked by white arrows). In contrast, no regions of high densities of PDs are found in the bulk of the sample with a Cu-rich stage (Fig. 1b). A small-grained top layer (Fig. 1b) is attributed to the final In–Ga–Se deposition stage (Fig. S1b, ESI†), which changes the composition back to Cu-poor. (Additional bright-field TEM images confirming the findings shown in Fig. 1a and b can be found in Fig. S2, ESI.†)

To confirm the presence of PDs, high-resolution TEM (HRTEM) was employed. Fig. 1c shows a large density and a large variety of PDs in the {112} planes in the In-rich part of the sample processed without the Cu-rich stage. As examples, two regions with PDs are marked and displayed as enlarged images in the insets: one showing two ordinary twin defects and the other exhibiting a narrow region with a hexagonal stacking sequence. The nature of individual PDs was studied in more detail by high-resolution scanning TEM (HR-STEM) (Fig. 1d–h). These measurements show additional types of PDs, such as twin faults (ABCBA), intrinsic stacking faults (ABC_BC), extrinsic stacking faults (ABC***B***ABC), and two irregular PDs, *i.e.*, defects that do not feature a mere cubic or hexagonal close-packed type stacking. All these extended defects have in common that they disturb the proper stacking of the {112} planes of the chalcopyrite structure.

Similar types of PDs were also found in the sample processed with a Cu-rich stage, but Fig. 1a and b show that the density of PDs is strongly reduced in the sample grown with the Cu-rich stage compared to the one grown without the Cu-rich stage. We note that the sample processed with the Cu-rich stage was exposed to the process temperature of 430 °C for a longer time than the sample without the Cu-rich stage. Therefore, from investigations on these samples alone it is unclear whether the annihilation of PDs is induced by the Cu-rich stage itself, or rather by the longer annealing time. In Section 2.4 it will be demonstrated that thermal annealing alone is not sufficient

Published on 18 April 2016. Downloaded by TU Berlin - Universitaetsbibl on 18/05/2017 14:53:02.

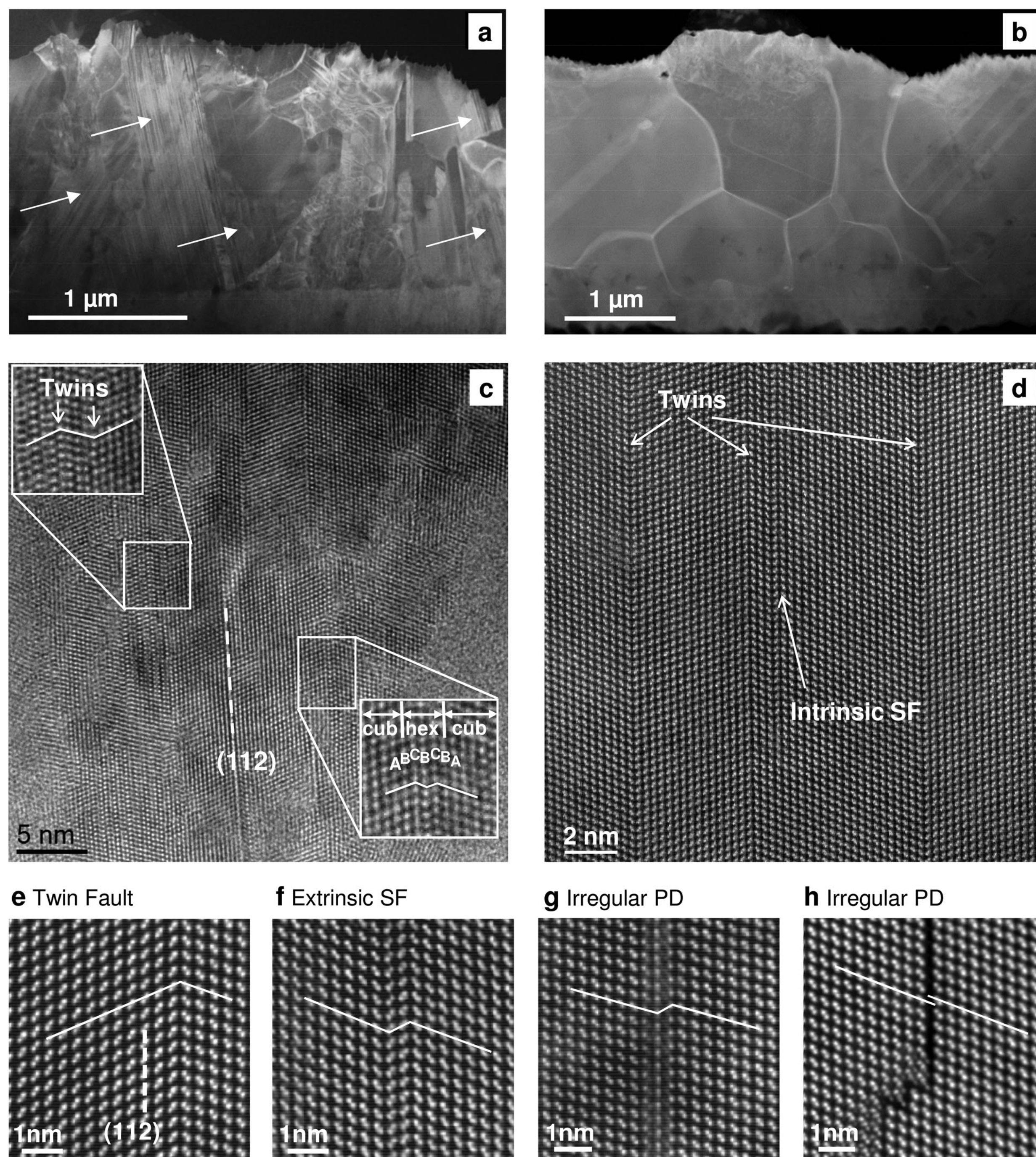

Fig. 1 (a and b) STEM-LAADF images of the sample that was synthesized (a) without and (b) with a Cu-rich process stage. (c) High-resolution TEM (HRTEM) image from the middle part of the CIGSe sample that was processed without a Cu-rich stage. (d–h) Detailed high-resolution scanning TEM (HR-STEM) images of various planar defects: (d) twin faults and an intrinsic stacking fault (SF), (e) a twin fault, (f) an extrinsic SF, (g) and (h) irregular planar defects (PD). All images in (c–h) show ⟨110⟩ projections.

to annihilate the PDs and that complete PD annihilation takes place at the transition from Cu-poor to Cu-rich film composition.

2.2 Electronic characterization

The presence of the various PDs in the Cu-poor grown CIGSe film raises the question whether they have an influence on the electronic properties of the film and hence whether their presence is problematic for the fabrication of high-performance solar cells. A twin or stacking fault imposes only small deviations from the anion–cation bond length, presumably without causing deep states in the band gap as proposed by Yan *et al.* for $CuInSe_2$.[34] In contrast, the irregular PDs in Fig. 1g and h show larger bond length deviations from the ideal lattice and

 This journal is © The Royal Society of Chemistry 2016

Published on 18 April 2016. Downloaded by TU Berlin - Universitaetsbibl on 18/05/2017 14:53:02.

can thus be expected to have stronger effects on the electronic structure.

To gain direct experimental insight into the electronic properties of PDs, we performed conductive atomic force microscopy (C-AFM), as well as scanning tunneling microscopy (STM) and scanning tunneling spectroscopy (STS). AFM topography and friction images obtained on the surface of the sample processed without a Cu-rich stage show contrasts that can be attributed to PDs within CIGSe grains (circles in Fig. 2a and b). C-AFM measurements suggest that the effect of the PDs on the local transport properties is negligible as there is no indication of the formation of a potential barrier at the PDs (Fig. 2c). This is concluded from the fact that negative (opposite to the bias voltage) currents were not observed, indicating that there is no band-bending at the PDs.[35,36] However, the STS data show a higher density of states (DOS) at some PDs relative to the grain bulk, as depicted in Fig. 2d, while others show the same DOS at the grain bulk (see Fig. S3, ESI†). We investigated several areas with PDs and found that about 40% of the PDs show an increased DOS, while about 60% did not show such an effect. These results confirm that some of the PDs may indeed be electronically benign, as predicted.[34] However, the increased DOS for around 40% of the PDs suggests that the high density of PDs seen in Fig. 1a and c will bring about an increase in charge carrier recombination. Hence, we conclude that for highest efficiencies it is essential to avoid or remove PDs during absorber fabrication.

The AFM and STS results in Fig. 2 were obtained on the surface of the sample processed without a Cu-rich stage. We also found some PDs at the surface of the sample processed with a Cu-rich stage using AFM and STM (Fig. S4, ESI†). This could be due to the fact that the surface of this sample grew under Cu-poor conditions during the end of the 3rd process stage. However, the presence of such PDs found in the STM measurements was much scarcer than in the sample without the Cu-rich stage. This and the reduced PD density in the bulk observed by STEM-LAADF compared to the sample grown without the Cu-rich stage (Fig. 1a and b) imply that in the sample with the Cu-rich stage the overall effect on recombination in the absorber film should be significantly reduced.

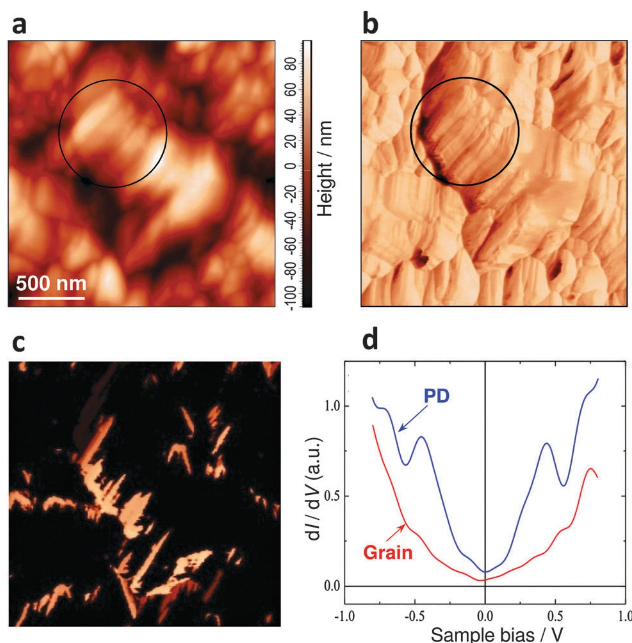

Fig. 2 Electronic characterization on the surface of the sample processed without a Cu-rich stage. (a) Topography and (b) lateral force measured by atomic force microscopy (AFM). (c) Current at 20 meV measured by C-AFM under AFM illumination at the same area as (a and b). (d) Scanning tunneling spectroscopy (STS) measurement at a planar defect (PD, blue curve) and on a grain bulk region far away from visible PDs (red curve).

2.3 Planar defect analysis by X-ray diffraction

Due to the small sample volumes analyzed by TEM, a doubt remains whether the apparent reduction of PDs in the sample processed with the Cu-rich stage (Fig. 1b) is representative. In contrast to TEM, X-ray diffraction – which is known to be sensitive to the presence of stacking faults[15,37,38] – probes much larger sample volumes in the order of 0.1 mm^3. We simulated the expected effect of various PD types, similar to those shown in Fig. 1c–h, using the XRD simulation software DIFFaX[37] with a pseudo-cubic approximation ($2a = c$).[15] The simulation results are presented in Fig. 3a. The simulations show that all observed types of {112} PDs lead to a broadening of the 112 reflection and an additional maximum at around $2\theta = 25°$ (marked as PD) with a sharp shoulder to the left. While variations of the profile shape for different defect types can be seen, qualitatively the various PDs have similar effects on the diffraction pattern.

The additional maximum (marked as PD in Fig. 3a) is not part of the chalcopyrite symmetry. Its presence is caused by the disturbance of this symmetry in an array of lattice planes with Miller indices

$$(h,k,l)_{\text{tetr}} = (h,h,2\cdot(h \pm 2))_{\text{tetr}}$$

(or $(h,k,l)_{\text{cub}} = (h,h,h \pm 2)_{\text{cub}}$ in the cubic sphalerite structure), where h can also take fractions of natural numbers. These two arrays of disturbed lattice plane symmetries become visible in a Fourier transformation (Fig. 3b) of the HRTEM image shown in Fig. 1c. The Fourier transform shows characteristic streaking along the $(h,h,h \pm 2)_{\text{cub}}$ line. For comparison, a Fourier transform of a model lattice image (see Fig. S5, ESI†) with twin faults in the $(111)_{\text{cub}}$ plane is depicted in Fig. 3c, showing similar streaking, with the upper streak along the $(h,k,l)_{\text{cub}} = (h,h,h+2)_{\text{cub}}$ line and the lower streak along the $(h,k,l)_{\text{cub}} = (h,h,h-2)_{\text{cub}}$ line. Circular integration of the intensity of the model Fourier transform around the origin leads to the line profile depicted in Fig. 3d, which qualitatively resembles the profile of XRD simulation in Fig. 3a. The sharp edge to the left of the $\{111\}_{\text{cub}}$ maximum corresponds to the distance of the nearest Se–Se neighbors in the $(111)_{\text{cub}}$ plane (or $(112)_{\text{tetr}}$ plane), which is the distance of planes with $\frac{3}{2}d_{112,\text{cub}}$ (or $\frac{3}{2}d_{114,\text{tetr}}$) (which corresponds to $d_{100,\text{hex}}$ in the hexagonal close-packed wurtzite-type structure[39]). This is the largest distance of the symmetry-disturbed planes in real space, *i.e.* the shortest distance from the center to the streak in the Fourier transform in Fig. 3b and c. This explains why the circularly integrated intensity in Fig. 3d

Published on 18 April 2016. Downloaded by TU Berlin - Universitaetsbibl on 18/05/2017 14:53:02.

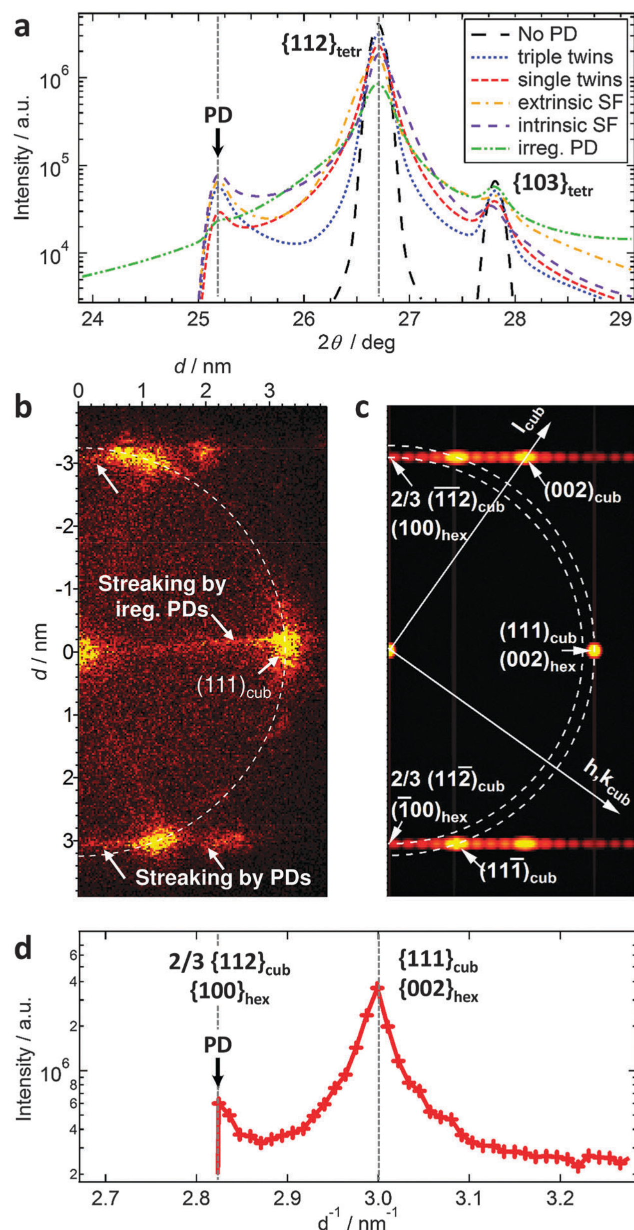

Fig. 3 (a) Simulated XRD patterns for various types of planar defects, which were observed by TEM as shown in Fig. 1. The simulations were performed using the software DIFFaX[37] and show a characteristic feature attributed to planar defects (PD). (b) Fast Fourier transformation (FFT) of the HRTEM image in Fig. 1c. (c) FFT of the corresponding fcc model lattice image with twin faults in the $(111)_{cub}$ plane with a fault probability of 6%. To enlarge the spots for better visibility, a smoothing function was run on the FFT pattern. (d) Circularly integrated intensity of the Fourier transform corresponding to the one in (c). (For reduced scattering, the integration was performed on a FFT pattern of a lattice image with 6000 $(111)_{cub}$ planes, whereas for (c) an image with only 300 planes was used.) The dashed vertical lines in (d) correspond to the radii of the dashed circles in (c).

shows a sudden intensity cut-off at this position towards smaller *k*-values (*i.e.* smaller 2θ angles or larger lattice plane spacings). For the case of $CuInSe_2$, this distance is

$$\frac{3}{2}d_{114,\mathrm{tetr}} = \frac{3}{2}\sqrt{1/a^2 + 1/a^2 + (4/c)^2} = 0.3556\ \mathrm{nm},$$

which corresponds to a XRD peak position of $2\theta = 25.018°$ (with $a = 0.5781$ nm and $b = 1.16422$ nm, ref. 40). The corresponding cut-off position is marked as a vertical dashed line in Fig. 3a and d.

Grazing incidence XRD (GIXRD) measurements performed on the sample processed without the Cu-rich stage clearly show this additional diffraction feature (Fig. 4a, black arrow) predicted for PDs by XRD simulations. The left vertical line in Fig. 4a marks the calculated cut-off position corresponding to $\frac{3}{2}d_{114,\mathrm{tetr}}$, which was also added to Fig. 3a and d. In contrast, this PD signal is absent in the sample processed with the Cu-rich stage (Fig. 4b). (Here, the additional reflections at higher angles can be attributed to the top layer with increased Ga concentration deposited in the 3rd stage of the process, see Fig. S1b, ESI.†)

It is important to note that a preferential grain orientation in the film can strongly influence the measured intensity of the PD signal. Therefore, from Fig. 4b we cannot be absolutely sure that the PD signal disappeared for all possible grain orientations. Texture analysis reveals that both sample types – processed without and with the Cu-rich stage – have a {220}/{204} fiber texture, *i.e.* the majority of grains have a lattice orientation with {220} or {204} planes parallel to the surface (Fig. 4c and d). Consequently, the pole figure for the PD signal of the sample processed without the Cu-rich stage also shows a strong orientation dependence with a maximum at an inclination angle of 30° (Fig. 4e), which is in accordance with a {220}/{204} fiber texture as visualized in Fig. 4g. In contrast, the pole figure for the PD signal of the sample processed with the Cu-rich stage is completely flat, confirming that for all grain orientations the density of PDs is reduced below the XRD resolution limit.

2.4 Dynamics of the planar defect annihilation

From the previous observations by *ex situ* analysis it remains unclear whether the disappearance of PDs in the sample with the Cu-rich stage is due to the intermediate Cu-rich composition during the deposition process – or whether the defects just annealed due to the longer processing time. Therefore, we performed a second co-evaporation process without the Cu-rich stage, but now with an additional annealing time, such that the thermal history equaled that for the sample grown with the Cu-rich stage (see Methods for details on the process). GIXRD measurements on samples from this process without the Cu-rich stage but with additional annealing still show a strong PD signal (Fig. S6, ESI†), revealing that the annihilation of the PDs is indeed induced by the compositional changes during the continued part of the process with the Cu-rich stage.

Still it remains unclear at which point during the process with the Cu-rich stage the PDs annihilate. To answer this question, we recorded diffraction signals in real time during CIGSe film synthesis by synchrotron-based energy-dispersive X-ray diffraction (EDXRD) in a co-evaporation chamber that was tailor-made for *in situ* X-ray analysis at the polychromatic synchrotron beamline EDDI at BESSY II.[30] Time-resolved EDXRD intensities around the CIGSe 112 reflection during Cu–Se evaporation (the 2nd stage of the three-stage process) are plotted and color-coded as functions of photon energy and Cu–Se deposition time in Fig. 5a. In EDXRD

 This journal is © The Royal Society of Chemistry 2016

Published on 18 April 2016. Downloaded by TU Berlin - Universitaetsbibl on 18/05/2017 14:53:02.

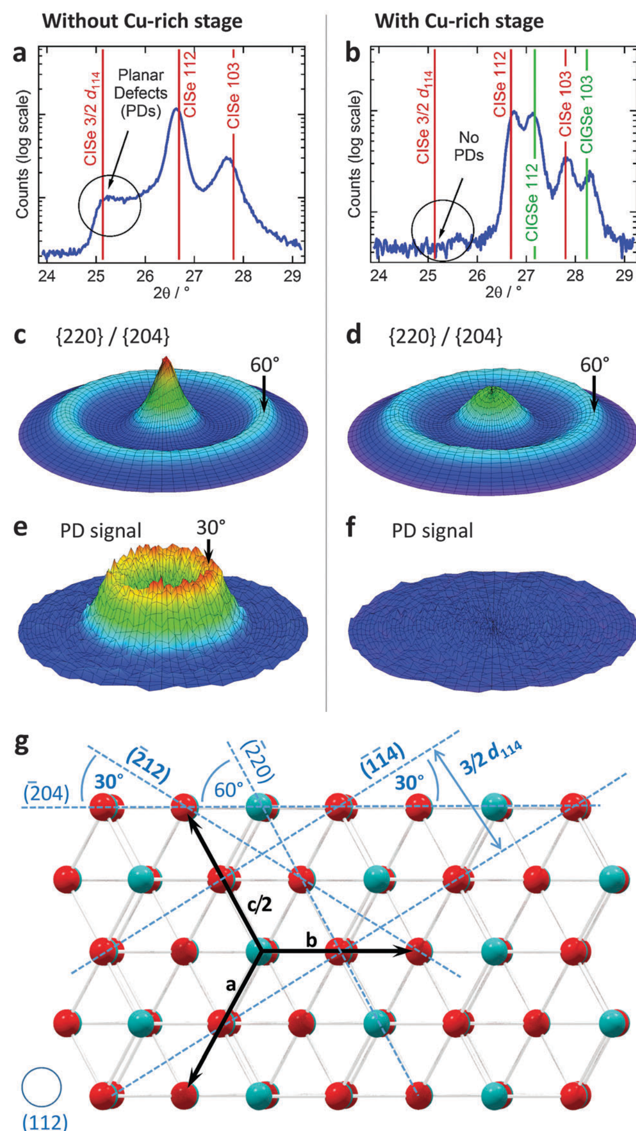

Fig. 4 *Ex situ* grazing incidence XRD (GIXRD) measured on the sample processed (a) without and (b) with a Cu-rich process stage. Pole figures for the {220}/{204} reflection (c) and the planar defect (PD) signal (e) for the sample without a Cu-rich stage. (d and f) show the corresponding pole figures for the sample processed with a Cu-rich stage. The arrows mark positions at which maxima are expected for a perfect {220}/{204} fiber texture, as schematically shown in (g). The image plane in (g) is parallel to the (112) plane.

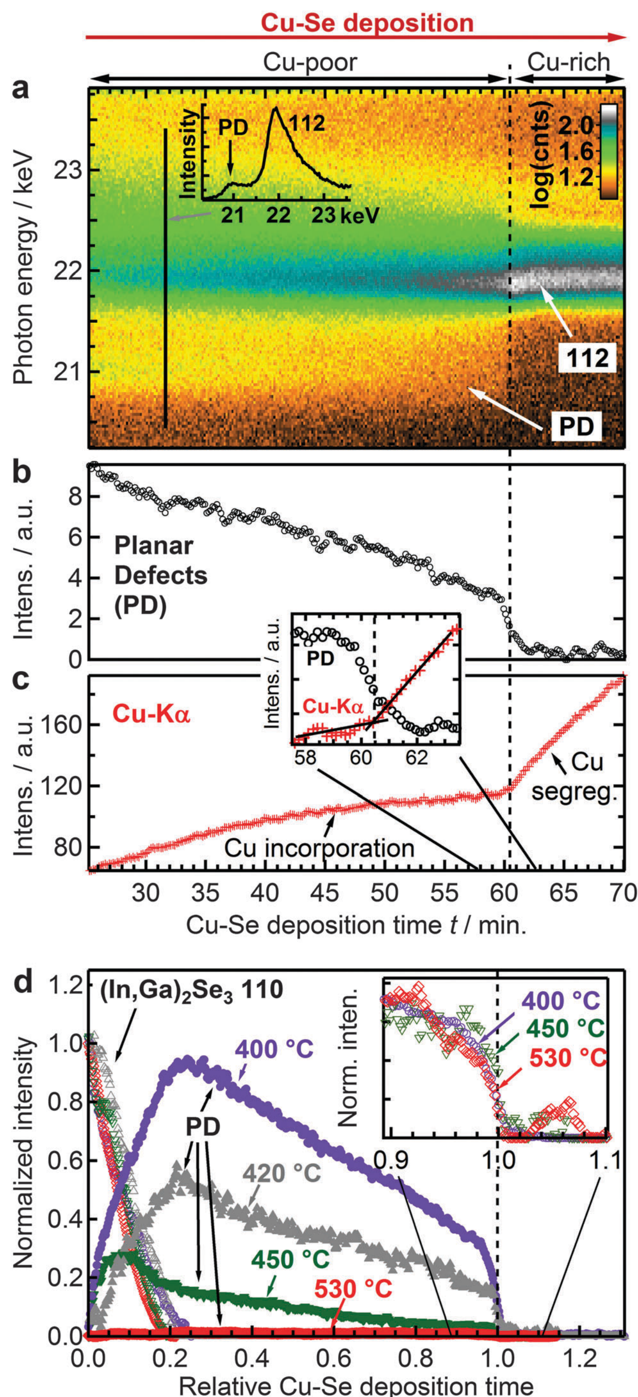

Fig. 5 Real-time EDXRD/XRF analysis of planar defect annihilation in a Cu–In–Ga–Se film during Cu–Se deposition. (a) Color-coded EDXRD spectra as a function of energy and Cu–Se deposition time, showing the CIGSe 112 diffraction signal and the planar defect (PD) signal. Inset: a spectrum recorded at the point in time marked by the black vertical line. Integral intensity of (b) the PD signal and (c) the simultaneously recorded Cu-Kα fluorescence. (d) Normalized intensities of the $(In,Ga)_2Se_3$ 110 and the PD signal intensities during Cu–Se deposition onto $(In,Ga)_2Se_3$ films at various substrate temperatures. The vertical dashed line marks the Cu-poor to Cu-rich transition. The inset shows an enlarged view around the transition (note the different normalization).

the same structural information is obtained as in conventional angle-dispersive XRD (for more details see Methods). The peak at around 22 keV corresponds to the CIGSe 112 reflection. The broad shoulder towards lower energies (marked by PD in Fig. 5a) corresponds to the PD signal that was also seen in *ex situ* XRD in Fig. 4a. The inset in Fig. 5a presents data extracted from an EDXRD spectrum at the point in time marked by the vertical black line, showing a similar profile of the PD signal as was seen in *ex situ* XRD in Fig. 4a. The PD signal shows a clear decrease in intensity during Cu–Se deposition (Fig. 5a and b) – with a slow decrease up to $t \approx 60$ min, followed by a rapid drop down to around zero within 3 minutes (see the inset).

Published on 18 April 2016. Downloaded by TU Berlin - Universitaetsbibl on 18/05/2017 14:53:02.

To correlate the decrease of the PD signal with the Cu incorporation into the film, the intensity of simultaneously recorded Cu fluorescence (Cu-Kα) is plotted in Fig. 5c. Due to the shallow incidence and exit angles of the EDXRD/XRF setup (see Methods), the fluorescence signals provide time-resolved information about elemental depth distributions.[41] While the slow increase of Cu-Kα up to $t \approx 60$ min can be explained by a near homogenous incorporation of Cu into the film, the increased slope starting at the vertical dashed line reveals the onset of Cu–Se segregation at the surface of the film,[30,42] which is expected as soon as the film is Cu-saturated.[42] It can be seen that the fast drop of the PD signal starts shortly before the onset of Cu–Se segregation. We can distinguish between two PD annihilation regimes – a slow one taking place at Cu-poor composition (*i.e.*, before the onset of Cu segregation), and a fast one taking place near stoichiometric composition. This finding provides direct evidence that the Cu-poor to Cu-rich transition plays a unique role in the defect reduction of CIGSe films at low growth temperatures.

But is the Cu-poor to Cu-rich transition really necessary to annihilate the PDs? The slow decrease of the PD density during the Cu-poor stage suggests that by tuning the process parameters, possibly a minimization of PD abundance may be achieved even before the film turns Cu-rich. For a thermally activated mechanism, increasing the temperature or prolonging the process time by reducing the Cu–Se deposition rate should lead to reduced PD concentration before Cu-rich to Cu-poor transition is reached.

To test this possibility and to gain further insight into the PD annihilation, we varied the substrate temperature and the Cu deposition rate. Fig. 5d shows that the PD signal intensities are strongly influenced by the substrate temperature during Cu–Se deposition. For all temperatures, the PD signal starts to increase during the transition of the $(In,Ga)_2Se_3$ phase to Cu–In–Ga–Se (Fig. S7, ESI†). It can be seen from Fig. 5d that the maximum intensity of the PD signal is strongly reduced when increasing the temperature from 400 °C to 530 °C. However, a close examination reveals that even for a substrate temperature of 530 °C, a faint PD signal is still present at Cu-poor composition, which – similar to the lower temperatures – decreases during the Cu-poor to Cu-rich transition (inset in Fig. 5d). Moreover, for 500 °C and 530 °C – in contrast to 400 °C – no significant signal intensity decrease can be observed between 0.2 and 0.9 relative Cu–Se deposition time (see Fig. S8, ESI†). At a substrate temperature of 530 °C, reducing the Cu evaporation rate – and hence prolonging the annealing time – did not have any effect on the intensity of the PD signal before the transition. A reduction of the Cu rate only prolonged the time until the PD signal disappeared at the Cu-poor to Cu-rich transition (Fig. S9, ESI†). Therefore, we can exclude the possibility that the defects completely anneal due to the longer processing time at temperatures of up to 530 °C. We conclude that even at higher substrate temperatures of up to around 530 °C – commonly used for deposition on soda-lime glass substrates – the Cu-poor to Cu-rich transition leads to a reduction of the density of PDs, which is likely to be a prerequisite for achieving world-record efficiencies.

2.5 Mechanism of planar defect annihilation

Two distinct mechanisms can lead to the annihilation of PDs: defects anneal within a grain (*e.g.* by motion of dislocations to the grain boundaries[27]), or defect-poor grains grow at the expense of defect-rich grains.[21] In both cases, the energy stored in the defects may act as a driving force for the annihilation (Fig. 6).

In the first case, when the PDs anneal within the grains, the energy barrier will be connected with the barrier for mechanisms such as dislocation gliding. However, for planar faults that go through entire grains – as seen in Fig. 1a (and Fig. S2b, ESI†) – the driving force for its motion should be small. Additionally, only small formation energies for stacking faults and twins were predicted for $CuInSe_2$ and $CuGaSe_2$.[43]

In the second case, when the defects are removed by grain growth, the energy barrier for defect annihilation will be similar to the barrier for grain boundary motion.[13,14] It is known that the grain size increases with temperature,[44,45] as expected for thermally activated grain growth, and that – in particular at lower temperatures – the grain size increases at the Cu-poor to Cu-rich transition.[13–15,21,44] Also the STEM-LAADF images in Fig. 1a and b showed that the grain size increased when a Cu-rich growth stage was performed. For CIGSe the extraction of the evolution of crystal domain sizes from diffraction peak widths is not reliable due to the Ga gradient, which also influences the peak width. However, since in a similar process without Ga the width of the 112 peak decreased with decreasing PD signal and remained constant afterwards,[30,42] we conclude that the grain growth takes place during planar fault annihilation.

The acceleration of the annihilation rate at the Cu-poor to Cu-rich transition can then be explained by a lowering of the activation energy for grain boundary mobility.[13,14,42,44,46] The facts that the relative annihilation rate at the Cu-poor to Cu-rich transition is not influenced by temperature (inset in Fig. 5d) and that the annihilation rate is prolonged by reducing the Cu deposition rate (Fig. S9b, ESI†) suggest that the barrier is flattened by Cu saturation (Fig. 6) and that the velocity of PD annihilation is determined only by the Cu deposition rate.

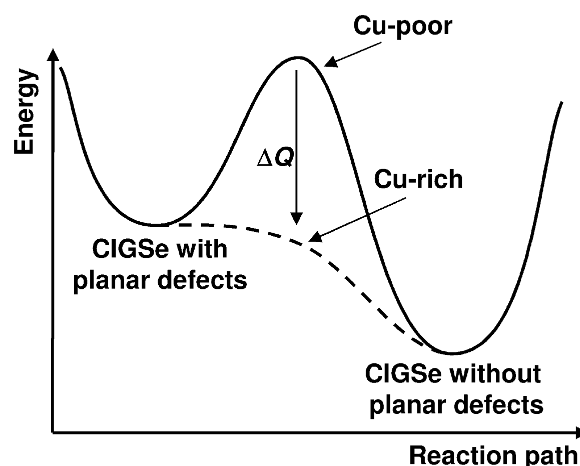

Fig. 6 Schematic drawing of the energy barrier between CIGSe with planar defects and CIGSe without planar defects.

 This journal is © The Royal Society of Chemistry 2016

Published on 18 April 2016. Downloaded by TU Berlin - Universitaetsbibl on 18/05/2017 14:53:02.

The complete disappearance of the PD signal at the transition from Cu-poor to Cu-rich can, however, not be explained solely by normal grain growth. In normal grain growth, larger grains grow by consuming smaller grains. If we assume that initially also large grains feature high densities of PDs, as seen in the STEM-LAADF images in Fig. 1a, normal grain growth would leave substantial amounts of PDs, which would still cause a detectable PD diffraction signal. Consequently, the observation that the PD signal completely disappears within the resolution of the XRD and EDXRD measurements strongly suggests that the film completely recrystallizes at the Cu-poor to Cu-rich transition. Besides grain boundary energy and strain energy,[42] the defect energies may act as additional driving force for the recrystallization, similar to a phase-transition-driven grain growth.[3]

3 Conclusions

In this paper we showed that a high density of planar defects is present in Cu-poor $Cu(In,Ga)Se_2$ absorber films synthesized by low-temperature co-evaporation, if the film was Cu-poor all along the growth. The planar defects quickly annihilate during Cu–Se deposition near the onset of Cu–Se segregation at the surface. While the defect formation can also be reduced by applying higher substrate temperatures, a detectable planar defect signal remains until Cu–Se segregation during the transition from the Cu-poor to the Cu-rich composition even at a substrate temperature of around 530 °C – a temperature commonly used for $Cu(In,Ga)Se_2$ co-evaporation on glass. Interestingly, the relative rate of defect annihilation at the transition does not depend on the substrate temperature, but instead it is controlled by the Cu-deposition rate. This has two important implications for the design of co-evaporation processes for high-efficiency CIGSe solar cell absorbers: first, if a process is performed without an intermediate Cu-rich stage, high substrate temperatures need to be applied to reduce the defect density. Second, if a process is performed with an intermediate Cu-rich stage, a reduction of the substrate temperature during Cu–Se deposition – in order to reduce energy consumption and enable usage of temperature-sensitive substrates – does not present a disadvantage in terms of defect density. The relevance of these findings for solar cell applications was demonstrated by the relationship found between the presence of the planar defects and the presence of electronic defect states, suggesting a lower recombination of the charge carriers and thus improved photovoltaic properties – especially open circuit voltage – of the material grown with a Cu-rich process stage.

4 Methods

Film synthesis

The *ex situ* analyzed CIGSe samples were synthesized in a three-stage-type process, using Mo-coated glass substrates with a SiN diffusion barrier to prevent uncontrolled Na diffusion from the glass into the film. Initially, two samples were processed together: in the 1st stage, Ga–Se and In–Se were subsequently deposited at 330 °C. In the 2nd stage, the temperature was increased to 430 °C and Cu–Se was deposited. When the integral Cu concentration reached $[Cu]/([In] + [Ga]) \approx 0.71$, *i.e.* before the integral film composition turned Cu-rich, the Cu–Se deposition was interrupted and the samples were allowed to cool down. After cooling down, one sample was taken out of the chamber (this sample is referred to as "without the Cu-rich stage"). The remaining sample in the chamber was heated up again to 430 °C and the second stage (Cu–Se deposition) was continued until the integral composition turned Cu-rich. Finally, in the third stage In, Ga and Se were deposited simultaneously until the integral composition turned back to Cu-poor with $[Cu]/([In] + [Ga]) \approx 0.81$ (this sample is referred to as "with the Cu-rich stage"). To test whether the PD annihilation is caused by the compositional changes during the continued process or by thermal annealing due to the longer processing time, we performed a second deposition process: this process was identical to the first one (described above), except that this time, after Cu–Se deposition was interrupted and one sample was taken out of the chamber, the process was continued without Cu–Se and In–Ga–Se deposition. Only the Se source was turned on and the remaining sample was kept at 430 °C as long as in the first process to ensure an identical thermal history of the samples from the first and the second process.

Ex situ characterization

TEM lamellae were prepared using a focused ion beam (FIB) Zeiss Crossbeam 1540XB instrument by a lift-out method for STEM-LAADF (Fig. 1a and b) and HR-STEM (Fig. 1c–h) analyses. TEM lamellae for HRTEM analysis (Fig. 1c) were prepared by conventional techniques using tripod polishing and subsequent ion-milling. The STEM-LAADF measurements were done at 200 kV on the Zeiss Sub-Electron-Volt Sub-Angstrom Microscope (SESAM). An annular detector with an inner semi-angle of 10 mrad was used for STEM-LAADF imaging. A JEOL 4000FX was operated at 400 kV acceleration voltage for the HRTEM measurements. The HR-STEM measurements were carried out at 100 kV on a Nion UltraSTEM 100 microscope equipped with a cold field emission gun, a Cs corrector and a Gatan Enfina spectrometer. The probe forming optics of the instrument were adjusted to create a probe with a diameter of 0.9 Å at a convergence semi-angle of 33 mrad, allowing atomic-resolution imaging of the CIGSe structure in the $\langle 110 \rangle$ projection. The HAADF detector semi-angular range was set to 85–185 mrad.

STM measurements were performed under ambient conditions. In some cases the samples were treated for 2 min with an aqueous KCN solution, and then washed with distilled water, in order to prevent surface oxidation. However, the results were not quantitatively different from samples that did not undergo this procedure. The STM topographic images were typically measured with the sample-bias and current set values of V = 1.5 V and I = 1 nA, whereas the tunneling I–V curves were acquired with set values (before disabling the feedback loop for spectrum acquisition) of V = 0.8 V and I = 0.5 nA. The dI/dV–V tunneling spectra, which are proportional to the local DOS,[47] were numerically derived from curves resulting by averaging over 50–100 I–V characteristics taken at a specific location, in each

Published on 18 April 2016. Downloaded by TU Berlin - Universitaetsbibl on 18/05/2017 14:53:02.

of which the current was recorded, and averaged over, 64 times for every bias value. AFM: the Mo layer served as a back-contact (counter electrode to the conductive AFM tip) in the C-AFM measurements. The C-AFM data were acquired under ambient conditions. The tip-sample contact area has a diameter of $\sim$10 nm. Therefore, with a typical current of 0.1 nA, the current density is $\sim$100 A cm^{-2}. (See ESI† for more details.)

XRD measurements were performed using a standard laboratory diffractometer XPert Pro MPD, with Cu-Kα radiation and a parallelizing incident beam mirror and a Kβ filter (Ni). The grazing-incidence angle was 3°. Pole figures were measured using a SEIFERT 5-circle diffractometer ETA with cobalt Kα radiation.

DIFFaX simulation

XRD profiles in the presence of planar defects were simulated using the software DIFFaX[37] with a pseudo-cubic approximation ($2a = c$) and a stoichiometric $CuInSe_2$ lattice (For more details, see ref. 15.)

In situ EDXRD/XRF

Real-time EDXRD/XRF analysis during co-evaporation was performed with polychromatic synchrotron radiation between 6 and 100 keV at the EDDI beamline at BESSY II, equipped with two energy-dispersive Ge detectors.[48] For EDXRD the energy-dispersive form of the Bragg equation – $d_{hkl} = hc/(2E_{hkl}\sin\theta)$ – applies. The diffraction angle was $2\theta = 9.722° \pm 0.002°$ (calibrated with 99.99% purity gold powder), and the inclination angle was $\Psi \approx 65°$. The angle between incident radiation and the sample surface was $\Omega_{in} = 2.62°$ and the angle between diffracted radiation and the sample surface was $\Omega_{out} = 1.50°$. (More details on the setup can be found in ref. 30 and 42.) For all *in situ* processes, Mo-coated glass substrates with a SiN diffusion barrier were used. For the 420 °C process, a complete three-stage-type process was performed in the *in situ* chamber, with sequential Ga–Se/In–Se/Ga–Se/In–Se deposition in the 1st stage at 330 °C, Cu–Se (2nd stage) and In–Ga–Se (3rd stage) at 420 °C.[49] For the other *in situ* processes the first stage was performed beforehand in a different chamber, finished with a pure Se capping. In the *in situ* chamber, the samples were heated up to 530 °C and subsequently the temperature was lowered to the respective value (400 °C, 450 °C, 500 °C, or 530 °C) before Cu–Se deposition was started. The Cu–Se deposition time up to the point of Cu–Se saturation took around 70–80 min.

Acknowledgements

The work was partly funded by the Helmholtz Virtual Institute HVI-520 "Microstructure Control for Thin-Film Solar Cells", and by the European Metrology Research Programme (EMRP) Project IND07 Thin Films and Project ThinErgy. The EMRP is jointly funded by the EMRP participating countries within EURAMET and the European Union. SuperSTEM is the U.K. National Facility for Aberration-Corrected STEM, supported by the Engineering and Physical Sciences Research Council (EPSRC). Special thanks go to Ulrike Bloek for TEM sample preparation, Matthias Meixner for help with the texture measurements, and to Guido Wagener, Jakob Lauche, Tim Münchenberg, Lars Steinkopf, and Ole Zander for support during the EDXRD beamtime.

References

1 R. C. Armstrong, C. Wolfram, K. P. de Jong, R. Gross, N. S. Lewis, B. Boardman, A. J. Ragauskas, K. Ehrhardt-Martinez, G. Crabtree and M. Ramana, *Nat. Energy*, 2016, **1**, 15020.
2 J. Pohl and K. Albe, *J. Appl. Phys.*, 2010, **108**, 023509.
3 R. Mainz, A. Singh, S. Levcenko, M. Klaus, C. Genzel, K. M. Ryan and T. Unold, *Nat. Commun.*, 2014, **5**, 3133.
4 P. K. Nayak, G. Garcia-Belmonte, A. Kahn, J. Bisquert and D. Cahen, *Energy Environ. Sci.*, 2012, **5**, 6022–6039.
5 D. M. Powell, R. Fu, K. Horowitz, P. A. Basore, M. Woodhouse and T. Buonassisi, *Energy Environ. Sci.*, 2015, **8**, 3395–3408.
6 A. Chirila, S. Buecheler, F. Pianezzi, P. Bloesch, C. Gretener, A. R. Uhl, C. Fella, L. Kranz, J. Perrenoud, S. Seyrling, R. Verma, S. Nishiwaki, Y. E. Romanyuk, G. Bilger and A. N. Tiwari, *Nat. Mater.*, 2011, **10**, 857–861.
7 A. Chirila, P. Reinhard, F. Pianezzi, P. Bloesch, A. R. Uhl, C. Fella, L. Kranz, D. Keller, C. Gretener, H. Hagendorfer, D. Jaeger, R. Erni, S. Nishiwaki, S. Buecheler and A. N. Tiwari, *Nat. Mater.*, 2013, **12**, 1107–1111.
8 A. M. Gabor, J. R. Tuttle, D. S. Albin, M. A. Contreras, R. Noufi and A. M. Hermann, *Appl. Phys. Lett.*, 1994, **65**, 198–200.
9 L. Gütay, D. Regesch, J. K. Larsen, Y. Aida, V. Depredurand and S. Siebentritt, *Appl. Phys. Lett.*, 2011, **99**, 151912.
10 R. Caballero, C. Kaufmann, V. Efimova, T. Rissom, V. Hoffmann and H. Schock, *Prog. Photovolt.: Res. Appl.*, 2013, **21**, 30–46.
11 R. Klenk, T. Walter, H.-W. Schock and D. Cahen, *Adv. Mater.*, 1993, **5**, 114–119.
12 J. Kessler, C. Chityuttakan, J. Lu, J. Schöldström and L. Stolt, *Prog. Photovolt.: Res. Appl.*, 2003, **11**, 319–331.
13 N. Barreau, T. Painchaud, F. Couzinié-Devy, L. Arzel and J. Kessler, *Acta Mater.*, 2010, **58**, 5572–5577.
14 H. Rodriguez-Alvarez, R. Mainz, B. Marsen, D. Abou-Ras and H. W. Schock, *J. Appl. Crystallogr.*, 2010, **43**, 1053–1061.
15 H. Rodriguez-Alvarez, N. Barreau, C. Kaufmann, A. Weber, M. Klaus, T. Painchaud, H.-W. Schock and R. Mainz, *Acta Mater.*, 2013, **61**, 4347–4353.
16 I. Repins, N. Vora, C. Beall, S.-H. Wei, Y. Yan, M. Romero, G. Teeter, H. Du, B. To, M. Young and R. Noufi, *MRS Proceedings*, 2011, **1324**, mrss11-1324-d17-01, DOI: 10.1557/opl.2011.844.
17 I. Repins, C. Beall, N. Vora, C. DeHart, D. Kuciauskas, P. Dippo, B. To, J. Mann, W.-C. Hsu, A. Goodrich and R. Noufi, *Sol. Energy Mater. Sol. Cells*, 2012, **101**, 154–159.
18 M. Nakamura, Y. Kouji, Y. Chiba, H. Hakuma, T. Kobayashi and T. Nakada, Photovoltaic Specialists Conference (PVSC), 2013 IEEE 39th, 2013, pp. 0849–0852.
19 R. Mainz, A. Weber, H. Rodriguez-Alvarez, S. Levcencu, M. Klaus, P. Pistor, R. Klenk and H. Schock, *Prog. Photovolt.: Res. Appl.*, 2015, **23**, 1131–1143.

 This journal is © The Royal Society of Chemistry 2016

20 I. Repins, M. A. Contreras, B. Egaas, C. DeHart, J. Scharf, C. L. Perkins, B. To and R. Noufi, *Prog. Photovolt.: Res. Appl.*, 2008, **16**, 235–239.
21 H. Stange, S. Brunken, H. Hempel, H. Rodriguez-Alvarez, N. Schäfer, D. Greiner, A. Scheu, J. Lauche, C. A. Kaufmann, T. Unold, D. Abou-Ras and R. Mainz, *Appl. Phys. Lett.*, 2015, **107**, 152103.
22 T. Wada, T. Negami and M. Nishitani, *J. Mater. Res.*, 1994, **9**, 658–662.
23 S. S. Schmidt, D. Abou-Ras, S. Sadewasser, W. Yin, C. Feng and Y. Yan, *Phys. Rev. Lett.*, 2012, **109**, 095506.
24 J. Dietrich, D. Abou-Ras, T. Rissom, T. Unold, H. Schock and C. Boit, *IEEE J. Photovolt.*, 2012, **2**, 364–370.
25 C. Lei, C.-M. Li, A. Rockett, I. M. Robertson and W. Shafarman, *MRS Proceedings*, Symposium F – Thin-Film Compound Semiconductor Photovoltaics, 2005, p. F4.3.1.
26 J. Ge, J. Jiang, P. Yang, C. Peng, Z. Huang, S. Zuo, L. Yang and J. Chu, *Sol. Energy Mater. Sol. Cells*, 2014, **125**, 20–26.
27 R. Sinclair, F. A. Ponce, T. Yamashita, D. J. Smith, R. A. Camps, L. A. Freeman, S. J. Erasmus, W. C. Nixon, K. C. A. Smith and C. J. D. Catto, *Nature*, 1982, **298**, 127–131.
28 H. Zheng, J. Wang, J. Y. Huang, A. Cao and S. X. Mao, *Phys. Rev. Lett.*, 2012, **109**, 225501.
29 J. Wei Wang, S. Narayanan, J. Yu Huang, Z. Zhang, T. Zhu and S. X. Mao, *Nat. Commun.*, 2013, **4**, 3340.
30 H. Rodriguez-Alvarez, A. Weber, J. Lauche, C. A. Kaufmann, T. Rissom, D. Greiner, M. Klaus, T. Unold, C. Genzel, H.-W. Schock and R. Mainz, *Adv. Energy Mater.*, 2013, **3**, 1381–1387.
31 P. Pistor, S. Zahedi-Azad, S. Hartnauer, L. A. Wägele, E. Jarzembowski and R. Scheer, *Phys. Status Solidi A*, 2015, **212**, 1897–1904.
32 Z. Yu, D. A. Muller and J. Silcox, *J. Appl. Phys.*, 2004, **95**, 3362–3371.
33 Y. Zhu, X. Liao and X. Wu, *Prog. Mater. Sci.*, 2012, **57**, 1–62.
34 Y. Yan, K. Jones, C. Jiang, X. Wu, R. Noufi and M. Al-Jassim, *Phys. B*, 2007, **401–402**, 25–32.
35 D. Azulay, O. Millo, I. Balberg, H.-W. Schock, I. Visoly-Fisher and D. Cahen, *Sol. Energy Mater. Sol. Cells*, 2007, **91**, 85–90.
36 D. Azulay, I. Balberg and O. Millo, *Phys. Rev. Lett.*, 2012, **108**, 076603.
37 M. M. J. Treacy, J. M. Newsam and M. W. Deem, *Proc. R. Soc. London, Ser. A*, 1991, **433**, 499–520.
38 L. Balogh, G. Ribarik and T. Ungar, *J. Appl. Phys.*, 2006, **100**, 023512.
39 F.-J. Fan, L. Wu and S.-H. Yu, *Energy Environ. Sci.*, 2014, **7**, 190–208.
40 K. Knight, *Mater. Res. Bull.*, 1992, **27**, 161–167.
41 R. Mainz and R. Klenk, *J. Appl. Phys.*, 2011, **109**, 123515.
42 R. Mainz, H. Rodriguez-Alvarez, M. Klaus, D. Thomas, J. Lauche, A. Weber, M. D. Heinemann, S. Brunken, D. Greiner, C. A. Kaufmann, T. Unold, H.-W. Schock and C. Genzel, *Phys. Rev. B: Condens. Matter Mater. Phys.*, 2015, **92**, 155310.
43 N. I. Medvedeva, E. V. Shalaeva, M. V. Kuznetsov and M. V. Yakushev, *Phys. Rev. B: Condens. Matter Mater. Phys.*, 2006, **73**, 035207.
44 T. Schlenker, M. L. Valero, H. Schock and J. Werner, *J. Cryst. Growth*, 2004, **264**, 178–183.
45 P. Salome, A. Hultqvist, V. Fjällström, B. Vermang, M. Edoff, B. Aitken, K. Zhang, K. Fuller and C. K. Williams, *Sol. Energy Mater. Sol. Cells*, 2014, **123**, 166–170.
46 F. Couzinie-Devy, N. Barreau and J. Kessler, *Prog. Photovolt.: Res. Appl.*, 2011, **19**, 527–536.
47 R. Wiesendanger, *Scanning Probe Microscopy and Spectroscopy*, Cambridge University Press, 1994.
48 C. Genzel, I. A. Denks, R. Coelho, D. Thomas, R. Mainz, D. Apel and M. Klaus, *J. Strain Anal. Eng. Des.*, 2011, **46**, 615–625.
49 C. Kaufmann, R. Caballero, T. Unold, R. Hesse, R. Klenk, S. Schorr, M. Nichterwitz and H.-W. Schock, *Sol. Energy Mater. Sol. Cells*, 2009, **93**, 859–863.

Published on 18 April 2016. Downloaded by TU Berlin - Universitaetsbibl on 18/05/2017 14:53:02.